

# A linear smoothed polygonal scaled boundary element method with consistent one-point integration scheme

Xiupeng Nie<sup>a,b</sup>, Degao Zou<sup>a,b,\*</sup>, Kai Chen<sup>a,b,\*</sup>, Jingmao Liu<sup>a,b</sup>, Shanlin Tian<sup>a,b</sup>

<sup>a</sup> The State Key Laboratory of Coastal and Offshore Engineering, Dalian University of Technology, Dalian, Liaoning 116024, China

<sup>b</sup> School of Infrastructure Engineering, Dalian University of Technology, Dalian, Liaoning 116024, China

## ARTICLE INFO

### Keywords:

SBFEM  
Polygon  
Strain smoothing technique  
Linear consistency  
One-point integration

## ABSTRACT

The computational efficiency of SBFEM is closely related to the number of integration points in the element domain. This paper proposes the linearly consistent one-point integration scheme for two-dimensional (2D) polygonal SBFEM, designed to enhance its computational efficiency. By incorporating the linear strain smoothing technique and introducing higher-order derivatives via Taylor's expansion, the proposed method reduces the number of integration points to one per sub-triangle of polygon, significantly reducing the computational cost compared to conventional integration schemes. The essence of the proposed method lies in correcting the derivatives of the nodal shape functions at the one integration point of the geometric center by the discrete form of the divergence theorem, numerical stabilization is achieved by introducing higher-order terms through Taylor's expansion. Several benchmark problems are employed to validate the accuracy and the robustness of the proposed method, the results demonstrate that the proposed one-point integration scheme achieves comparable accuracy to the three integration points while significantly reducing computational costs by 45%-60%. This advancement not only improves the efficiency of SBFEM but also broadens its applicability to large-scale engineering problems requiring high computational performance.

## 1. Introduction

In the field of engineering and computational mechanics, the finite element method (FEM) has been widely adopted as a crucial numerical approach to analyze the mechanical behavior of complex structures, such as seismic structure-media interactions (Zhao et al., 2020; Zhang et al., 2021a) and crack propagation (Zhao et al., 2018; Du et al., 2020), etc. However, with advances in engineering technology and increasing demands for computational accuracy and efficiency, the limitations of traditional FEM have become increasingly evident in specific application scenarios. In the numerical simulation of structures characterized by complex geometry, the inherent disadvantage in mesh discretization flexibility of FEM may adversely affect its computational accuracy and efficiency.

In this context, the semi-analytical scaled boundary finite element method (SBFEM) has garnered significant academic attention. SBFEM is proposed by Song and Wolf (1997, 1998), and its core idea is to transform the solution domain from the traditional full-space discretization to the discretization on the boundary only, meanwhile, the scaled boundary coordinate system is applied to describe the problem geometry and

physical properties. This innovative method unifies the beneficial aspects of FEM and the boundary element method, which not only retains the feasibility of the FEM in dealing with nonlinear problem, but also inherits the advantages of the BEM in reducing the dimension of the problem and simplifying the mesh generation process (Song et al., 2018; Ooi et al., 2020), this unique feature enables SBFEM to competently compute polygonal elements with an arbitrary number of nodes. In addition, SBFEM achieves an analytical solution in the radial direction (Song et al., 2010; Ooi et al., 2016), potentially offering higher accuracy than FEM and providing more effective solutions for certain complex problems.

In recent years, Song has thoroughly researched and developed the basic theory of SBFEM, including its mathematical foundation (Song and Wolf, 1997), numerical stability (Song 2004) and accuracy analysis (Song 2009). The series of work has provided solid theoretical support for the method and promoted its application in several research fields. Ooi et al. (2015, 2016, 2018, 2020) have further advanced this foundation through theoretical developments in SBFEM, enabling its application to a wider range of problems. Chen et al. (2017, 2018a, 2018b) applied SBFEM to the earth and rock dam engineering, offering a highly

\* Corresponding authors at: The State Key Laboratory of Coastal and Offshore Engineering, Dalian University of Technology, Dalian, Liaoning 116024, China.  
E-mail addresses: [zoudegao@dlut.edu.cn](mailto:zoudegao@dlut.edu.cn) (D. Zou), [chenkai@dlut.edu.cn](mailto:chenkai@dlut.edu.cn) (K. Chen).

accurate and flexible solution for large-scale engineering applications. Chen et al. (2024) and Nie et al. (2024a, 2024b) extended the single element order type in SBFEM to mixed-order element types between first- and second-order, this advancement greatly broadened the diversity of element libraries supported by SBFEM. To analyze wave phenomena in infinite domains, Zhao and his colleagues (Zhang et al., 2023a, 2023b, 2024a, 2024b, 2024c) introduced a scaled-boundary perfectly matched layer approach, which has shown high reliability and robustness in engineering applications. Du et al. (Du et al., 2023, Zhang et al., 2019, 2021b) utilized SBFEM to model crack propagation problems, numerical results indicate that the presented technique exhibits enhanced precision and computational performance. In addition to the research mentioned above, SBFEM has also been successfully applied to the double-phase-field algorithm (Zhuo et al., 2025), Cosserat continuum analysis (Chen et al., 2021, Nie et al., 2024c), and free vibration analysis (Liu et al., 2021, Ye et al., 2023), among others.

Despite its numerous advantages, SBFEM still faces some challenges in practical applications. Among these challenges, a major research focus is optimizing computational efficiency without compromising accuracy. This challenge stems from the boundary scaling process in SBFEM, where the elemental domain of an  $n$ -sided polygon is typically subdivided into  $n$  sub-triangles. To ensure computational stability, it is necessary to allocate 3 integration points to each sub-triangle. As a result, a total of  $3n$  integration points are required per element, which undoubtedly poses a significant challenge to computational efficiency and calculation resource consumption. In FEM, the direct use of a single integration within an element, i.e. the reduced integration, gives rise to a series of numerical instability issues, including the hourglass mode (Flanagan and Belytschko, 1981) and a diminished capacity to capture high gradient regions (Zienkiewicz et al., 1971). Thus, an optimal integration scheme for SBFEM should strike a balance between computational accuracy and efficiency.

In the context of mesh-free methods, recent research has focused on strategies to reduce integration points, leading to approaches such as stress-point integration (Fries and Belytschko, 2008; Duan and Belytschko, 2009), support domain integration (Kie et al., 2006; Liu and Belytschko, 2010), and one-point integration schemes (Wang et al., 2019; Duan et al., 2012a). Among these, consistent one-point integration has emerged as a stable and efficient method for reducing computational costs in mesh-free analysis. This method employs only a single integration point per subdomain to evaluate the Galerkin weak form. Building on the strain smoothing technique and the divergence theorem, Duan et al. (2012b) proposed a consistency framework for mesh-free nodal derivatives. Within this framework, an integration scheme called the consistent three integration scheme (QC3) is proposed, which accurately reproduces linear strain fields by correcting nodal derivatives at the integration point. Afterwards, Duan et al. (2012a) incorporated higher-order derivatives into the discrete divergence consistency method through a Taylor's series expansion, enabling the transformation of QC3 into a one-point integration scheme.

In this paper, the linearly consistent one-point integration scheme is adapted from the mesh-free method to 2D SBFEM. Only one integration point is required per sub-triangle domain within the element. The proposed method employs a linear smoothing function for weighted averaging of the compatible strain, followed by the derivation of smoothed nodal derivatives at the geometric center of the sub-triangle domain via the discrete form of the divergence theorem. To ensure numerical stability and accuracy, a stabilization technique corrects the derivatives of the nodal shape functions at the one integration point through Taylor's expansion. The stiffness matrix and the strain-displacement matrix are assembled through the Taylor's expansion form of the derivatives of the nodal shape functions. The accuracy, efficiency, and applicability are investigated through several benchmark examples in both elastic and elastoplastic problems.

The structure of this paper is as follows: In Section 2, the theoretical formulation of the 2D SBFEM is briefly reviewed. Section 3 discusses the

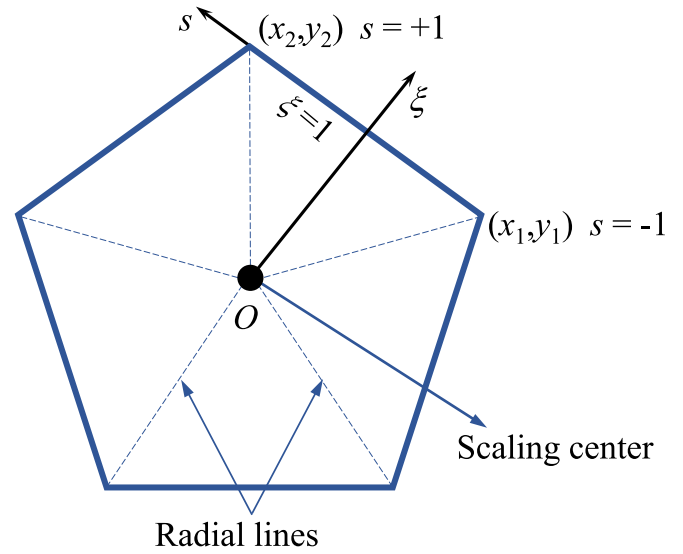


Fig. 1. Local coordinate diagram in SBFEM.

use of linear smoothing technique to calculate corrected nodal shape function derivatives, along with the one-point integration scheme in the SBFEM system. Section 4 provides numerical examples to validate the accuracy and efficiency of the proposed method for different problems. Section 5 further illustrates its practical application in geotechnical structures. Finally, the conclusions are summarized in Section 6.

## 2. Theoretical derivation of 2D SBFEM

### 2.1. Coordinates transformation

In 2D SBFEM, polygons with an arbitrary number of edges are supported, provided that their geometry satisfies a specified scaling requirement, which involves selecting an interior scaling center  $O$  (Fig. 1) from which the entire boundary is directly visible. A unique local coordinate system  $(\xi, s)$  is adopted in the SBFEM theory, as shown in Fig. 1, where  $\xi$  represents the radial coordinate, ranging from 0 to 1, and  $s$  represents the circumferential coordinate of each edge with a value ranging from  $-1$  to  $1$ . A point in the Cartesian coordinate system  $\{x, y\}$  can be represented in the scaled boundary coordinate system  $(\xi, s)$  as:

$$x(\xi, s) = x_0 + \xi \mathbf{N}(s) \mathbf{x}_b \quad (1)$$

$$y(\xi, s) = y_0 + \xi \mathbf{N}(s) \mathbf{y}_b \quad (2)$$

$$\mathbf{N}(s) = [\mathbf{N}_1(s), \mathbf{N}_2(s), \mathbf{N}_3(s), \dots, \mathbf{N}_m(s)] \quad (3)$$

where  $x_0, y_0$  are scaling center coordinates,  $x_b, y_b$  are the nodal coordinates vector of the line element on the boundary, and  $\mathbf{N}(s)$  is the shape function matrix of the line element with  $m$  nodes.

### 2.2. Scaled boundary general solution

The approximate displacement at any point within the scaled coordinate system of a sub-triangle domain can be expressed as:

$$\mathbf{u}(\xi, s) = \mathbf{N}_u(s) \mathbf{u}(\xi) \quad (4)$$

where  $\mathbf{u}(\xi)$  are the analytical function of nodal displacement along the radial line.  $\mathbf{N}_u(s)$  is the nodal shape function matrix, which is defined as:

$$\mathbf{N}_u(s) = \begin{bmatrix} \mathbf{N}_1(s) & 0 & \mathbf{N}_2(s) & 0 & \dots & 0 & \mathbf{N}_m(s) & 0 \\ 0 & \mathbf{N}_1(s) & 0 & \mathbf{N}_2(s) & 0 & \dots & 0 & \mathbf{N}_m(s) \end{bmatrix} \quad (5)$$

Following Galerkin's weighted residual method (Song and Wolf,

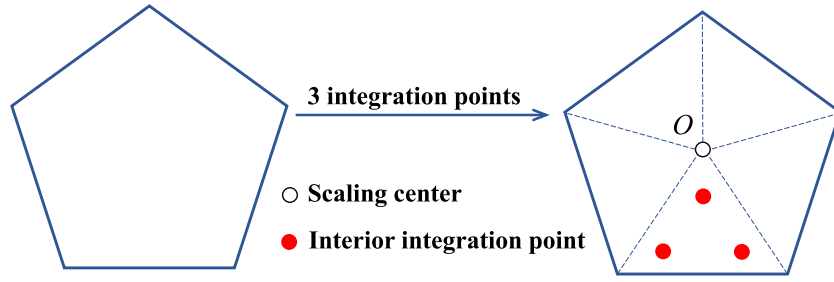


Fig. 2. The conventional integration scheme in SBFEM.

1997), the partial differential equations about the radial displacements functions  $u(\xi)$ , which are regarded as the SBFEM governing equation for displacement, can be formed and it is expressed as:

$$E_0 \xi^2 u(\xi)_{\xi\xi} + (E_0 + E_1 + E_1^T) \xi u(\xi)_{,\xi} - E_2 u(\xi) = 0 \quad (6)$$

where the coefficient matrices  $E_i$  ( $i = 0, 1, 2$ ), which is related to the geometry and material properties, are assembled from each subdomain, the equation can be rewritten as:

$$E_0 = \int_{-1}^{+1} B_1^T D B_1 |J| ds \quad (7a)$$

$$E_1 = \int_{-1}^{+1} B_2^T D B_1 |J| ds \quad (7b)$$

$$E_2 = \int_{-1}^{+1} B_2^T D B_2 |J| ds \quad (7c)$$

where  $B_1$  and  $B_2$  are strain–displacement matrices,  $J$  is the Jacobian matrix, they are defined as:

$$B_1 = b_1(s) N(s) \quad (8a)$$

$$B_2 = b_2(s) N(s)_{,s} \quad (8b)$$

$$J = \begin{bmatrix} N(s) x_b & N(s) y_b \\ N(s)_{,s} x_b & N(s)_{,s} y_b \end{bmatrix} \quad (8c)$$

By introducing an intermediate variable  $X(\xi)$ , the equation in Eq. (6) can be transformed into a first-order differential equation of the following form:

$$\xi X(\xi)_{,\xi} = -Z X(\xi) \quad (9)$$

$$X(\xi) = \begin{bmatrix} u(\xi) \\ q(\xi) \end{bmatrix} \quad (10)$$

where  $q(\xi)$  in Eq. (10) is analytical function related to the internal nodal forces, and it is equal to:

$$q(\xi) = E_0 \xi u(\xi)_{,\xi} + E_1^T u(\xi) \quad (11)$$

The Hamilton matrix  $Z$  is:

$$Z = \begin{bmatrix} E_0^{-1} E_1^T & -E_0^{-1} \\ -E_1 + E_1 E_0^{-1} E_1^T & -E_1 E_0^{-1} \end{bmatrix} \quad (12)$$

The block-diagonal Schur decomposition of matrix  $Z$  in Eq. (12) is performed, the Schur block results in the following equation:

$$Z \begin{bmatrix} \psi_u \\ \psi_q \end{bmatrix} = \begin{bmatrix} \psi_u \\ \psi_q \end{bmatrix} S \quad (13)$$

$$S = \begin{bmatrix} S_n & \\ & S_p \end{bmatrix} \quad (14)$$

with  $S$  being a diagonal matrix containing the real parts of the eigenvalues of the  $Z$ ,  $S_n$  and  $S_p$  contain the eigenvalues with negative and positive real parts which are sorted in ascending order.  $\psi_u$  and  $\psi_q$  are the eigenvectors of the  $Z$ . The general solution for displacement  $u(\xi)$  in Eq. (6) is derived from these solved variables and expressed as:

$$u(\xi) = \psi_u \xi^{-S_n} c \quad (15a)$$

$$q(\xi) = \psi_q \xi^{-S_n} c \quad (15b)$$

In Eq. (15), the integration constants  $c$  can be determined from the nodal displacement on the boundary  $u_b = u(\xi = 1)$ :

$$c = \psi_u^{-1} u_b \quad (16)$$

### 2.3. Scaled boundary shape functions

The radial displacement function  $u(\xi)$  can be first derived by substituting Eq. (16) into Eq. (15a):

$$u(\xi) = \psi_u \xi^{-S_n} \psi_u^{-1} u_b \quad (17)$$

The displacement field  $u(\xi, s)$  of the element in the scaled boundary coordinates can be expressed by substituting Eq. (17) into Eq. (4):

$$u(\xi, s) = N_u(\xi, s) \psi_u \xi^{-S_n} \psi_u^{-1} u_b \quad (18)$$

Eq. (18) can be expressed as the product of the shape function matrix  $\Phi(\xi, s)$  and the node displacement  $u_b$  as in FEM, such as:

$$u(\xi, s) = \Phi(\xi, s) u_b \quad (19)$$

where  $\Phi(\xi, s)$  is shape functions in the scaled boundary coordinates, which is defined as:

$$\Phi(\xi, s) = N_u(\xi, s) \psi_u \xi^{-S_n} \psi_u^{-1} \quad (20)$$

It is worth noting that, unlike the FEM, the shape function matrix  $\Phi(\xi, s)$  of the SBFEM is a full matrix with the form shown in Eq. (20).

$$\Phi = \begin{bmatrix} \Phi_{11} & \Phi_{12} & \Phi_{13} & \Phi_{14} & \dots & \Phi_{1(2m-1)} & \Phi_{1(2m)} \\ \Phi_{21} & \Phi_{22} & \Phi_{23} & \Phi_{24} & \dots & \Phi_{2(2m-1)} & \Phi_{2(2m)} \end{bmatrix} \quad (21)$$

### 3. One-point integration scheme in SBFEM system

In current SBFEM research, the commonly used traditional integration scheme for linear elements is to arrange 3 integration points for each sub-triangle domain of the element, as shown in Fig. 2. In this section, we extend the recently developed linearly consistent one-point integration scheme proposed by Duan et al. (2012a) for mesh-free methods to SBFEM system, in this way, the number of integration points required in each sub-triangle domain can be reduced to one, and the specific implementation process is shown below.

#### 3.1. Linear strain smoothing technique

First, in 2D SBFEM, the compatible strain field  $\epsilon(x)$  within the

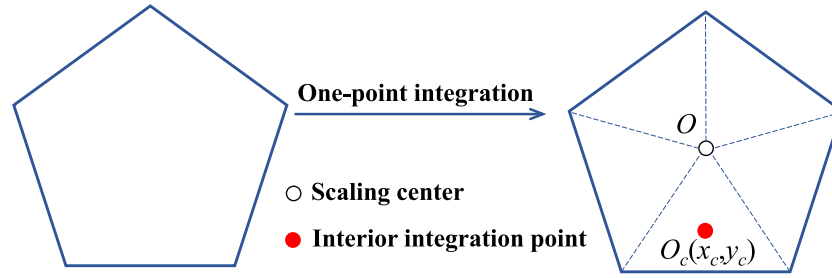


Fig. 3. The proposed one-point integration scheme in SBFEM.

element domain can be represented in the form of a Cartesian coordinate system as:

$$\epsilon(x) = B(x)u_b \quad (22)$$

where

$$B(x) = \begin{bmatrix} \Phi_{11,x} & \Phi_{12,x} & \dots & \Phi_{1(2m),x} \\ \Phi_{21,y} & \Phi_{22,y} & \dots & \Phi_{2(2m),y} \\ \Phi_{11,y} + \Phi_{21,x} & \Phi_{12,y} + \Phi_{22,x} & \dots & \Phi_{1(2m),y} + \Phi_{2(2m),x} \end{bmatrix} \quad (23)$$

After, within the smoothed finite element method framework (Liu et al., 2007), the compatible strain field  $\epsilon(x)$  within the element domain is averaged through the application of a weighting function  $f(x)$ , thus leading to the derivation of a smoothed (corrected) strain field  $\tilde{\epsilon}(x)$  as expressed in the following equation.

$$\tilde{\epsilon}(x) = \int_{\Omega} \epsilon(x)f(x)dS \quad (24)$$

By writing Eq. (24) at the derivative level of the nodal shape function, it can be expressed by means of the divergence theorem as:

$$\int_{\Omega} \tilde{\Phi}_{ij,x}(x)f(x)dS = \int_{\Gamma} \Phi_{ij}(x)f(x)n_x d\Gamma - \int_{\Omega} \Phi_{ij}(x)f_{,x}(x)dS \quad (25)$$

in which, the linear smoothing function  $f(x) = [1 \ x \ y]^T$  is used for the calculation of the corrected derivatives of the shape function  $\tilde{\Phi}_{ij,x}(x)$ , this formula is the so-called discrete divergence consistency in the consistency framework (Gao et al., 2016). Notably, in the current stage of the computational model, each sub-triangle domain still needs to be configured with 3 integration points, and the adoption of one-point integration (i.e. reduced integration method) in the meshless method at this time will lead to a singularity in the calculation (Duan et al., 2014), while in FEM, the reduced integration method will lead to a decrease in computational accuracy (Hughes et al., 1978).

By considering higher-order derivatives  $\tilde{\Phi}_{ij,xx}(x), \tilde{\Phi}_{ij,xy}(x)$  of the corrected shape functions  $\tilde{\Phi}_{ij,x}(x)$  in the geometric center of the sub-domain, i.e.  $O_c(x_c, y_c)$  in the Fig. 3 in the form of Taylor's expansion, this instability can be avoided. The Taylor's expansion form of terms  $\tilde{\Phi}_{ij,x}(x)$ ,  $f(x)$  and  $\Phi_{ij}(x)$  are expressed as follows:

$$\tilde{\Phi}_{ij,x}(x) = \tilde{\Phi}_{ij,x}(O_c) + (x - x_c)\tilde{\Phi}_{ij,xx}(O_c) + (y - y_c)\tilde{\Phi}_{ij,xy}(O_c) + \text{H.O.T} \quad (26)$$

$$f(x) = f(O_c) + (x - x_c)f_{,x}(O_c) + (y - y_c)f_{,y}(O_c) + \text{H.O.T} \quad (27)$$

$$\begin{aligned} \Phi_{ij}(x) &= \Phi_{ij}(O_c) + (x - x_c)\Phi_{ij,x}(O_c) + (y - y_c)\Phi_{ij,y}(O_c) \\ &+ \frac{1}{2}(x - x_c)^2\Phi_{ij,xx}(O_c) + (x - x_c)(y - y_c)\Phi_{ij,xy}(O_c) \\ &+ \frac{1}{2}(y - y_c)^2\Phi_{ij,yy}(O_c) + \text{H.O.T} \end{aligned} \quad (28)$$

### 3.2. Solution of corrected shape functions

In Section 3.1,  $O_c(x_c, y_c)$  is the so-called *One-point integration*, as

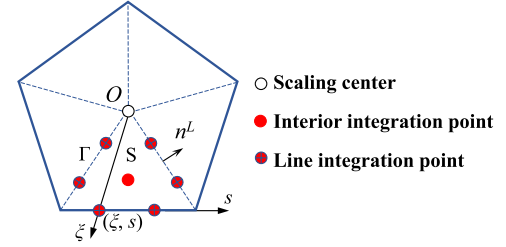


Fig. 4. Schematic diagram of one-point integration scheme for sub-triangle.

shown in Fig. 3. To solve the corrected first- and second-order partial derivatives of the shape functions at the one integration point, we first substitute Eq. (26) to (28) into Eq. (25), which gives:

$$\begin{aligned} f(O_c)A\tilde{\Phi}_{ij,x}(O_c) &+ [f_{,x}(O_c)I_{xx} + f_{,y}(O_c)I_{xy}] \tilde{\Phi}_{ij,xx}(O_c) \\ &+ [f_{,x}(O_c)I_{xy} + f_{,y}(O_c)I_{yy}] \tilde{\Phi}_{ij,xy}(O_c) \\ &= \int_{\Gamma} \Phi_{ij}(x)f(x)n_x dS - \left[ A\Phi_{ij}(O_c) + \frac{1}{2}I_{xx}\Phi_{ij,xx}(O_c) + I_{xy}\Phi_{ij,xy}(O_c) \right. \\ &\quad \left. + \frac{1}{2}I_{yy}\Phi_{ij,yy}(O_c) \right] \end{aligned} \quad (29)$$

where  $A$  is the area of the sub-triangle domain. The second-order moments related to the subdomain centre  $O_c$  are given by:

$$\begin{Bmatrix} I_{xx} \\ I_{xy} \\ I_{yy} \end{Bmatrix} = \int_{\Omega} \begin{Bmatrix} (x - x_c)^2 \\ (x - x_c)(y - y_c) \\ (y - y_c)^2 \end{Bmatrix} dS \quad (30)$$

The corresponding first-order area moments are as follows:

$$\begin{Bmatrix} I_x \\ I_y \end{Bmatrix} = \int_{\Omega} \begin{Bmatrix} (x - x_c) \\ (y - y_c) \end{Bmatrix} dS = 0 \quad (31)$$

For  $f(x) = [1 \ x \ y]^T$ , its corresponding terms in Taylor's expansion are:

$$f(O_c) = \begin{Bmatrix} 1 \\ x_c \\ y_c \end{Bmatrix}, \quad f_{,x}(O_c) = \begin{Bmatrix} 0 \\ 1 \\ 0 \end{Bmatrix}, \quad f_{,y}(O_c) = \begin{Bmatrix} 0 \\ 0 \\ 1 \end{Bmatrix} \quad (32)$$

The first term on the right side of Eq. (29) is integrated using 2 Gauss integration points (Fig. 4) on each edge, and substituting Eq. (32) into Eq. (29), a system of linear equations can be represented as:

$$\begin{bmatrix} A & 0 & 0 \\ Ax_c & I_{xx} & I_{xy} \\ Ay_c & I_{xy} & I_{yy} \end{bmatrix} \begin{bmatrix} \tilde{\Phi}_{ij,x}(O_c) \\ \tilde{\Phi}_{ij,xx}(O_c) \\ \tilde{\Phi}_{ij,xy}(O_c) \end{bmatrix} = \begin{bmatrix} F_{ij,1}^x \\ F_{ij,2}^x \\ F_{ij,3}^x \end{bmatrix} \quad (33)$$

where

$$\begin{bmatrix} F_{ij,1}^x \\ F_{ij,2}^x \\ F_{ij,3}^x \end{bmatrix} = \begin{bmatrix} \sum_{L=1}^3 \sum_{G=1}^{G_n} \Phi_{ij}(p_G) n_x^L w_G \\ \sum_{L=1}^3 \sum_{G=1}^{G_n} \Phi_{ij}(p_G) x_G n_x^L w_G - F_{\Omega} \\ \sum_{L=1}^3 \sum_{G=1}^{G_n} \Phi_{ij}(p_G) y_G n_x^L w_G \end{bmatrix} \quad (34)$$

with

$$F_{\Omega} = A\Phi_{ij}(O_c) + \frac{1}{2}I_{xx}\Phi_{ij,xx}(O_c) + I_{xy}\Phi_{ij,xy}(O_c) + \frac{1}{2}I_{yy}\Phi_{ij,yy}(O_c) \quad (35)$$

where  $\Phi_{ij}(O_c)$ ,  $\Phi_{ij,x}(O_c)$ ,  $\Phi_{ij,xx}(O_c)$  and  $\Phi_{ij,xy}(O_c)$  are the standard shape functions and its corrected derivatives which are obtained at the geometric center  $O_c(x_c, y_c)$  of the sub-triangle domain, and  $G$  is the number of line Gauss points on each side, for a linear element  $G_n = 2$ , while for a quadratic element  $G_n = 3$ .  $p_G$  is the line Gauss point,  $(x_G, y_G)$  and  $w_G$  are the line Gauss point coordinate and its weight along the boundary of the sub-triangle domain;  $n_x^L$  is the x-direction component of the unit normal vector of the line element in sub-triangle domain. In SBFEM, the derivatives of the shape function in natural coordinates involve a Jacobian transformation concerning the scaled boundary coordinate system, which is expressed as:

$$\begin{bmatrix} \frac{\partial}{\partial \xi} \\ \frac{\partial}{\partial \eta} \end{bmatrix} = \begin{bmatrix} \frac{\partial x}{\partial \xi} & \frac{\partial y}{\partial \xi} \\ \frac{\partial x}{\partial \eta} & \frac{\partial y}{\partial \eta} \end{bmatrix} \cdot \begin{bmatrix} \frac{\partial}{\partial x} \\ \frac{\partial}{\partial y} \end{bmatrix} = \mathbf{J} \cdot \begin{bmatrix} \frac{\partial}{\partial x} \\ \frac{\partial}{\partial y} \end{bmatrix} \quad (36)$$

By virtue of the Jacobian matrix, the first-order derivative of the shape function  $\Phi_{ij,x}(O_c)$  in the Cartesian coordinate system can be related to the first-order derivative  $\Phi_{ij,\xi}(O_c)$  and  $\Phi_{ij,\eta}(O_c)$  in the scaled boundary coordinate system with the following expression:

$$\begin{aligned} \Phi_{ij,x}(O_c) &= \frac{1}{|\mathbf{J}|} \left[ y(s)_{,s} \cdot \Phi_{ij,\xi} - \frac{1}{\xi} y(s) \cdot \Phi_{ij,\eta} \right] \\ \Phi_{ij,y}(O_c) &= \frac{1}{|\mathbf{J}|} \left[ -x(s)_{,s} \cdot \Phi_{ij,\xi} + \frac{1}{\xi} x(s) \cdot \Phi_{ij,\eta} \right] \end{aligned} \quad (37)$$

Based on Eq. (36) and (37), the second-order derivative of the shape function  $\Phi_{ij,xx}(O_c)$ ,  $\Phi_{ij,xy}(O_c)$  and  $\Phi_{ij,yy}(O_c)$  in the Cartesian coordinate system can be expressed as:

$$\begin{aligned} \Phi_{ij,xx}(O_c) &= \frac{1}{|\mathbf{J}|} \left[ y(s)_{,s} \cdot \frac{\partial \Phi_{ij,\xi}}{\partial x} - \frac{1}{\xi} y(s) \cdot \frac{\partial \Phi_{ij,\eta}}{\partial x} \right] \\ &= \frac{1}{|\mathbf{J}|^2} \left\{ y(s)_{,s}^2 \cdot \Phi_{ij,\xi\xi} - \frac{2}{\xi} y(s)_{,s} \cdot y(s)_{,\eta} \cdot \Phi_{ij,\xi\eta} + \frac{1}{\xi^2} y(s)^2 \cdot \Phi_{ij,\eta\eta} \right\} \end{aligned} \quad (38)$$

$$\begin{aligned} \Phi_{ij,xy}(O_c) &= \frac{1}{|\mathbf{J}|} \left[ y(s)_{,s} \cdot \frac{\partial \Phi_{ij,\xi}}{\partial y} - \frac{1}{\xi} y(s) \cdot \frac{\partial \Phi_{ij,\eta}}{\partial y} \right] \\ &= \frac{1}{|\mathbf{J}|^2} \left\{ -x(s)_{,s} \cdot y(s)_{,s} \cdot \Phi_{ij,\xi\xi} + \frac{1}{\xi} \left[ x(s)_{,s} \cdot y(s)_{,\eta} + x(s)_{,\eta} \cdot y(s)_{,s} \right] \cdot \Phi_{ij,\xi\eta} \right. \\ &\quad \left. - \frac{1}{\xi^2} x(s)_{,\eta} \cdot y(s)_{,\eta} \cdot \Phi_{ij,\eta\eta} \right\} \end{aligned} \quad (39)$$

$$\begin{aligned} \Phi_{ij,yy}(O_c) &= \frac{1}{|\mathbf{J}|} \left[ -x(s)_{,s} \cdot \frac{\partial \Phi_{ij,\xi}}{\partial y} + \frac{1}{\xi} x(s) \cdot \frac{\partial \Phi_{ij,\eta}}{\partial y} \right] \\ &= \frac{1}{|\mathbf{J}|^2} \left\{ x(s)_{,s}^2 \cdot \Phi_{ij,\xi\xi} - \frac{2}{\xi} x(s)_{,s} \cdot x(s)_{,\eta} \cdot \Phi_{ij,\xi\eta} + \frac{1}{\xi^2} x(s)^2 \cdot \Phi_{ij,\eta\eta} \right\} \end{aligned} \quad (40)$$

By observation, Eq. (34) can be analytically solved, and the corrected derivatives can be explicitly expressed as:

$$\begin{aligned} \tilde{\Phi}_{ij,x}(O_c) &= \frac{F_{ij,1}^x}{A} \\ \begin{Bmatrix} \tilde{\Phi}_{ij,xx}(O_c) \\ \tilde{\Phi}_{ij,xy}(O_c) \end{Bmatrix} &= \frac{1}{I_{xx}I_{yy} - I_{xy}^2} \begin{Bmatrix} I_{yy}(F_{ij,2}^x - F_{ij,1}^x x_c) - I_{xy}(F_{ij,3}^x - F_{ij,1}^x y_c) \\ I_{xx}(F_{ij,3}^x - F_{ij,1}^x y_c) - I_{xy}(F_{ij,2}^x - F_{ij,1}^x x_c) \end{Bmatrix} \end{aligned} \quad (41)$$

In a similar manner, the methodology for solving the derivatives in the y-direction is implemented as follows:

$$\begin{bmatrix} A & 0 & 0 \\ Ax_c & I_{xx} & I_{xy} \\ Ay_c & I_{xy} & I_{yy} \end{bmatrix} \begin{bmatrix} \tilde{\Phi}_{ij,y}(O_c) \\ \tilde{\Phi}_{ij,yx}(O_c) \\ \tilde{\Phi}_{ij,yy}(O_c) \end{bmatrix} = \begin{bmatrix} F_{ij,1}^y \\ F_{ij,2}^y \\ F_{ij,3}^y \end{bmatrix} \quad (42)$$

where

$$\begin{bmatrix} F_{ij,1}^y \\ F_{ij,2}^y \\ F_{ij,3}^y \end{bmatrix} = \begin{bmatrix} \sum_{L=1}^3 \sum_{G=1}^{G_n} \Phi_{ij}(p_G) n_y^L w_G \\ \sum_{L=1}^3 \sum_{G=1}^{G_n} \Phi_{ij}(p_G) x_G n_y^L w_G \\ \sum_{L=1}^3 \sum_{G=1}^{G_n} \Phi_{ij}(p_G) y_G n_y^L w_G - F_{\Omega} \end{bmatrix} \quad (43)$$

The variables in Eq. (43) are defined similarly to their x-direction counterparts above. The analytic solutions to Eq. (43) leads to:

$$\begin{aligned} \tilde{\Phi}_{ij,y}(O_c) &= \frac{F_{ij,1}^y}{A} \\ \begin{Bmatrix} \tilde{\Phi}_{ij,yx}(O_c) \\ \tilde{\Phi}_{ij,yy}(O_c) \end{Bmatrix} &= \frac{1}{I_{xx}I_{yy} - I_{xy}^2} \begin{Bmatrix} I_{yy}(F_{ij,2}^y - F_{ij,1}^y x_c) - I_{xy}(F_{ij,3}^y - F_{ij,1}^y y_c) \\ I_{xx}(F_{ij,3}^y - F_{ij,1}^y y_c) - I_{xy}(F_{ij,2}^y - F_{ij,1}^y x_c) \end{Bmatrix} \end{aligned} \quad (44)$$

### 3.3. Corrected stiffness matrix in SBFEM system

To incorporate high-order corrected derivatives into the solution equation, the corrected nodal derivatives are employed to determine the corrected stiffness matrix of the element, by this way, the corrected stiffness matrix is expanded in the form of a Taylor's expansion to obtain:

$$\begin{aligned} \tilde{\mathbf{K}} &= \int_{\Omega} \tilde{\mathbf{B}}^T \mathbf{D} \tilde{\mathbf{B}} d\Omega \\ &= \int_{\Omega} \left( \tilde{\mathbf{B}}^T + \tilde{\mathbf{B}}_x^T (\mathbf{x} - \mathbf{x}_c) + \tilde{\mathbf{B}}_y^T (\mathbf{y} - \mathbf{y}_c) \right) \mathbf{D} \left( \tilde{\mathbf{B}} + \tilde{\mathbf{B}}_x (\mathbf{x} - \mathbf{x}_c) + \tilde{\mathbf{B}}_y (\mathbf{y} - \mathbf{y}_c) \right) d\Omega \\ &= \mathbf{A} \tilde{\mathbf{B}}^T \mathbf{D} \tilde{\mathbf{B}} + I_{xx} \tilde{\mathbf{B}}_x^T \mathbf{D} \tilde{\mathbf{B}}_x + I_{yy} \tilde{\mathbf{B}}_y^T \mathbf{D} \tilde{\mathbf{B}}_y + I_{xy} \left( \tilde{\mathbf{B}}_x^T \mathbf{D} \tilde{\mathbf{B}}_y + \tilde{\mathbf{B}}_y^T \mathbf{D} \tilde{\mathbf{B}}_x \right) \end{aligned} \quad (45)$$

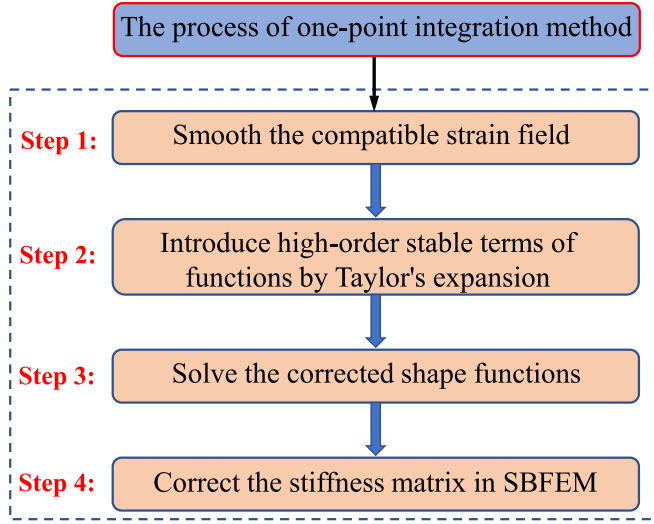


Fig. 5. Flowchart of the process of one-point integration scheme.

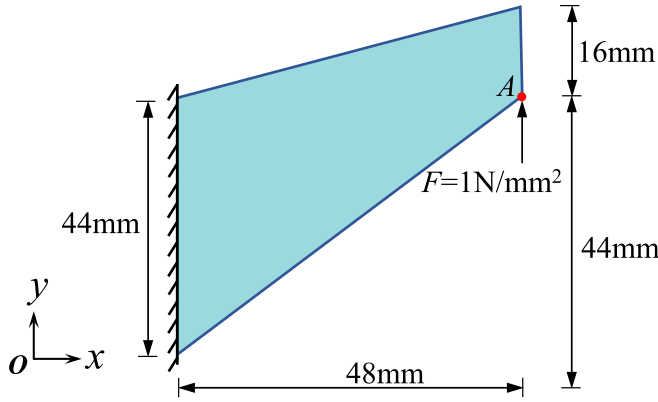


Fig. 6. Cook's membrane model.

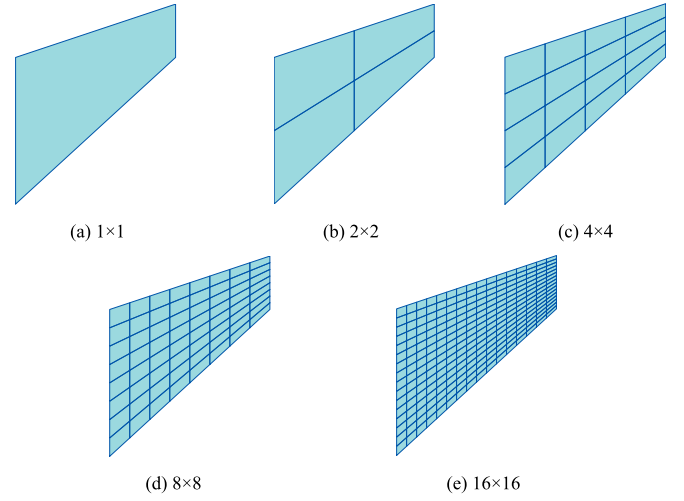


Fig. 7. Different mesh configurations of the cook's membrane.

Table 1

Detailed information on different integration schemes in SBFEM.

Integration scheme	Schematic diagram	Description
The full integration		Three integration points
The reduced integration		One integration point without strain smoothing technique
One-point integration in this paper		One integration point with strain smoothing technique

For enhanced comprehension of reader, the entire implementation process of the one-point integration scheme is presented in Fig. 5. Besides, the body force is re-solved in the same way as:

$$\tilde{\mathbf{B}} = \begin{bmatrix} \tilde{\Phi}_{11,x}(O_c) & \tilde{\Phi}_{12,x}(O_c) & \dots & \tilde{\Phi}_{1(2m),x}(O_c) \\ \tilde{\Phi}_{21,y}(O_c) & \tilde{\Phi}_{22,y}(O_c) & \dots & \tilde{\Phi}_{2(2m),y}(O_c) \\ \tilde{\Phi}_{11,y}(O_c) + \tilde{\Phi}_{21,x}(O_c) & \tilde{\Phi}_{12,y}(O_c) + \tilde{\Phi}_{22,x}(O_c) & \dots & \tilde{\Phi}_{1(2m),y}(O_c) + \tilde{\Phi}_{2(2m),x}(O_c) \end{bmatrix} \quad (46)$$

$$\begin{aligned} \tilde{\mathbf{B}}_x &= \begin{bmatrix} \tilde{\Phi}_{11,xx}(O_c) & \tilde{\Phi}_{12,xx}(O_c) & \dots & \tilde{\Phi}_{1(2m),xx}(O_c) \\ \tilde{\Phi}_{21,yx}(O_c) & \tilde{\Phi}_{22,yx}(O_c) & \dots & \tilde{\Phi}_{2(2m),yx}(O_c) \\ \tilde{\Phi}_{11,yx}(O_c) + \tilde{\Phi}_{21,xx}(O_c) & \tilde{\Phi}_{12,yx}(O_c) + \tilde{\Phi}_{22,xx}(O_c) & \dots & \tilde{\Phi}_{1(2m),yx}(O_c) + \tilde{\Phi}_{2(2m),xx}(O_c) \end{bmatrix}, \\ \tilde{\mathbf{B}}_y &= \begin{bmatrix} \tilde{\Phi}_{11,xy}(O_c) & \tilde{\Phi}_{12,xy}(O_c) & \dots & \tilde{\Phi}_{1(2m),xy}(O_c) \\ \tilde{\Phi}_{21,yy}(O_c) & \tilde{\Phi}_{22,yy}(O_c) & \dots & \tilde{\Phi}_{2(2m),yy}(O_c) \\ \tilde{\Phi}_{11,yy}(O_c) + \tilde{\Phi}_{21,xy}(O_c) & \tilde{\Phi}_{12,yy}(O_c) + \tilde{\Phi}_{22,xy}(O_c) & \dots & \tilde{\Phi}_{1(2m),yy}(O_c) + \tilde{\Phi}_{2(2m),xy}(O_c) \end{bmatrix} \end{aligned} \quad (47)$$



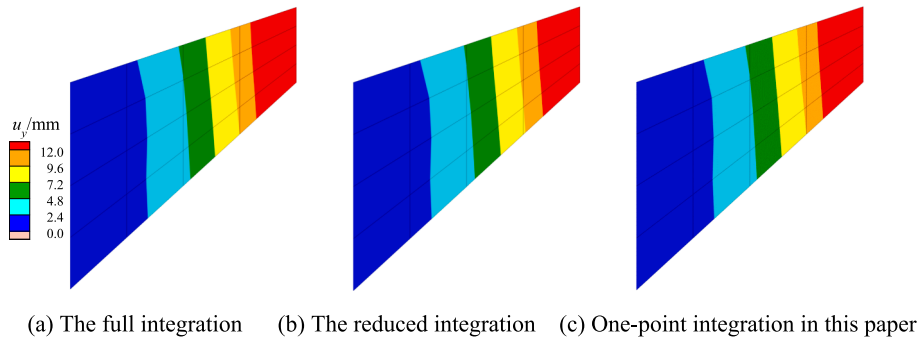


Fig. 8. Displacement results of  $4 \times 4$  mesh for different integration schemes.

Table 2

Displacement values of point A in cook's membrane.

Mesh	The full integration	The reduced integration		One-point integration in this paper	
	$u_y/\text{mm}$	$u_y/\text{mm}$	Error <sup>a</sup> / %	$u_y/\text{mm}$	Error <sup>b</sup> / %
$1 \times 1$	6.69	6.06	9.42	6.69	0
$2 \times 2$	12.71	11.57	8.97	12.69	0.16
$4 \times 4$	17.75	17.01	4.25	17.74	0.06
$8 \times 8$	22.28	21.73	2.47	22.27	0.04
$16 \times 16$	23.87	23.44	1.80	23.86	0.04
Reference	23.96				

<sup>a,b</sup>Errors of the reduced and one-point integration with the full integration for the same mesh.

$$f_b = \int_{\Omega} \Phi^T b d\Omega \quad (48)$$

$$= A \Phi^T b|_{O_c} + \frac{1}{2} I_c^{xx} \Phi_{xx}^T b|_{O_c} + I_c^{xy} \Phi_{xy}^T b|_{O_c} + \frac{1}{2} I_c^{yy} \Phi_{yy}^T b|_{O_c}$$

It is important to emphasize that the derivatives of the corrected nodal shape functions are specifically employed for the calculation of the stiffness matrix of the element, while the standard nodal derivatives remain applicable for the calculation of the body force terms.

## 4. Numerical examples

### 4.1. Bending Cook's membrane problem

#### 4.1.1. Model information

To illustrate the effectiveness and accuracy of the one-point integration scheme in this paper, the Cook's membrane problem (Cook et al., 1984), a widely used benchmark in computational mechanics, is employed. The geometry and boundary conditions of the Cook's membrane are illustrated in Fig. 6. The beam has a tapered shape with dimensions of 48 mm in length, 16 mm in height at the clamped end, and 44 mm in height at the free end. The left end of the beam is fully clamped, where all degrees of freedom are constrained, while a uniformly distributed shear load of  $F = 1\text{N/mm}^2$  is applied at the right end. The material behavior is assumed to follow linear elasticity, with a Young's modulus ( $E$ ) of 1 Pa and a Poisson's ratio ( $\nu$ ) of 0.333. The problem is solved under plane stress conditions.

#### 4.1.2. Mesh discretization

In this study, to ensure comprehensive evaluation of the computational accuracy and convergence characteristics, five distinct mesh configurations, each with a different number of elements, are utilized. See Fig. 7, the model is discretized into meshes with  $1 \times 1$ ,  $2 \times 2$ ,  $4 \times 4$ ,  $8 \times 8$  and  $16 \times 16$  quadrilateral elements respectively.

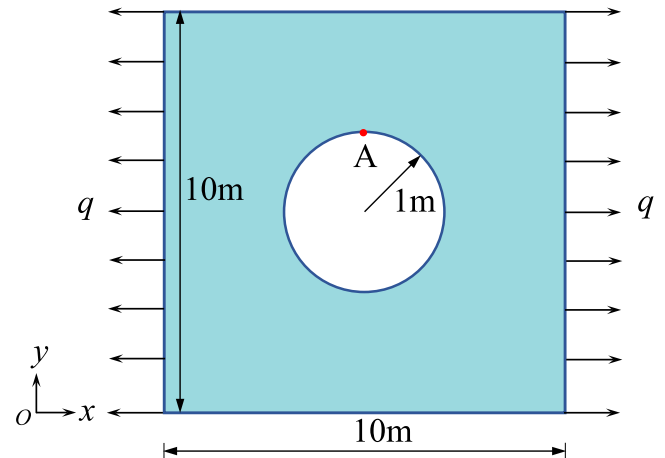


Fig. 9. Square plate with circular hole model.

#### 4.1.3. Calculated displacement results and comparison

In this section, the vertical displacements at the bottom-right corner (Point A) of the beam are systematically computed and compared with results obtained from other well-established integration schemes in SBFEM to validate the proposed method. The comparative analysis includes: ① The full integration scheme with three integration points; ② The reduced integration scheme, employing one integration point without strain smoothing technique; and ③ the proposed linearly consistent one-point integration scheme in this paper. The schematic diagrams of these different integration schemes are shown in the Table 1.

The finite element software GEODYNA 8.0 (Zou et al., 2022), which incorporates all the integration schemes listed in Table 1 for SBFEM, is utilized to perform the calculations on the aforementioned mesh configurations. The calculated displacement results for different integration schemes are shown in Fig. 8, and the displacement values of point A are summarized in Table 2, in which the reference solution is given by Long and Xu (1994). Here, we adopt the full integration scheme as a reference at the same mesh level. As shown in Table 2, as the mesh density increases, the displacement solutions corresponding to three different integration schemes gradually converge to the reference solution. When compared with the reference of the full integration scheme, the reduced integration scheme exhibits a certain degree of error, particularly in coarse mesh. Specifically, the relative error reaches approximately 10 % when only a single element is employed. The observed errors in the reduced integration scheme mainly result from numerical instability and insufficient sampling of the displacement field within the element. Consequently, these limitations may lead to inaccurate approximations of the integral terms in the formulation. In contrast, the one-point integration scheme maintains nearly the same computational accuracy as the full integration scheme, with all errors remaining very low and the

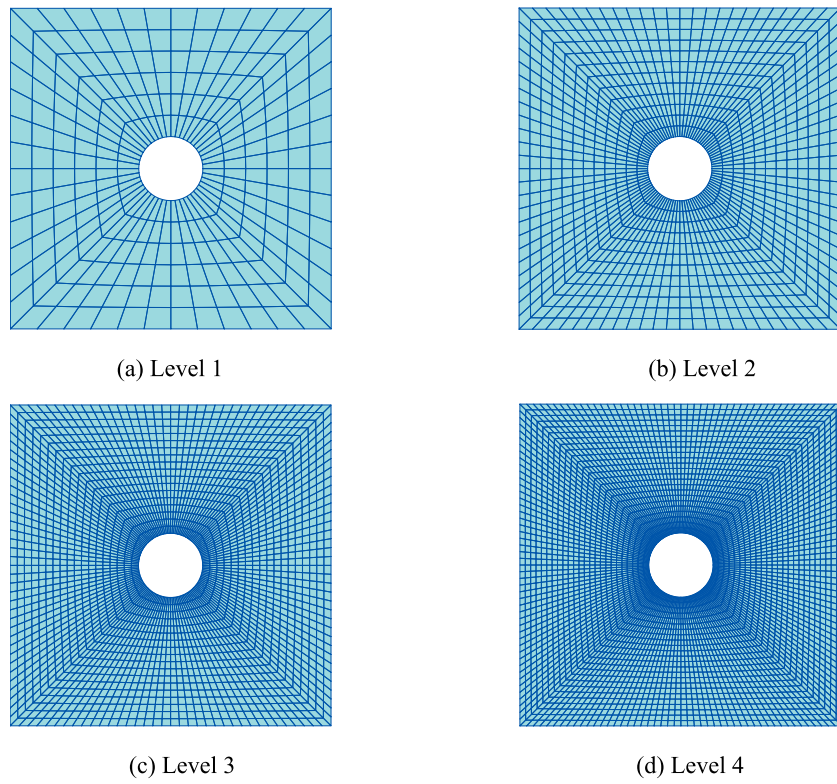


Fig. 10. Different mesh levels of the square plate.

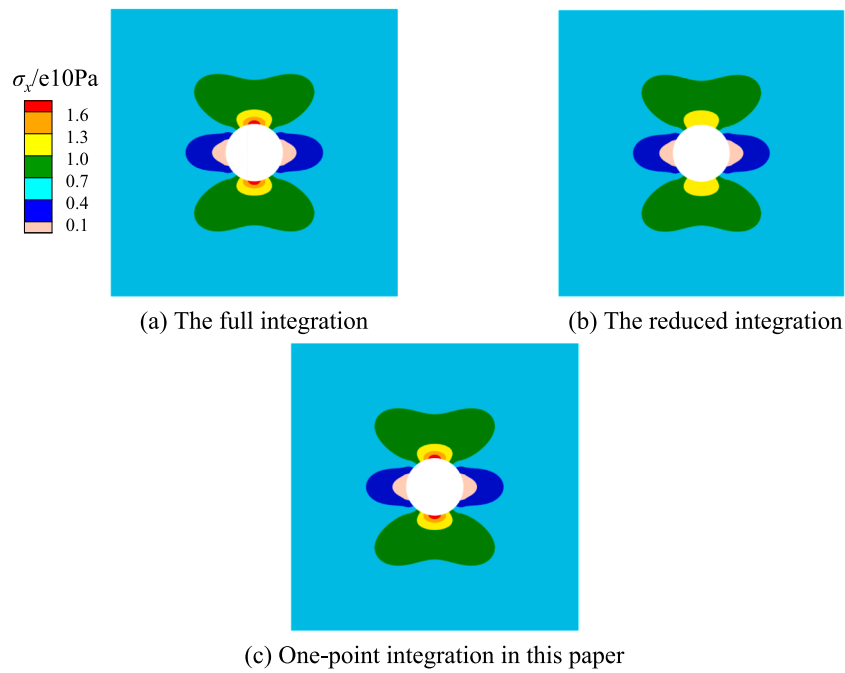


Fig. 11. Stress distribution of different integration schemes for level 4.

maximum error not exceeding 0.16 %. This demonstrates that the one-point integration scheme has good effectiveness and accuracy in simulating bending problems.

It is worth noting that reduced integration schemes do not exhibit significant errors in comparison to the other two integration schemes. This observation stems from the 'reduced' integration being performed solely within each sub-triangle domain, while the total number of

integration points in the  $n$ -sided element remains  $n$ . Therefore, the use of the reduced integration scheme does not lead to significantly poor computational results.

#### 4.2. Square plate with circular hole

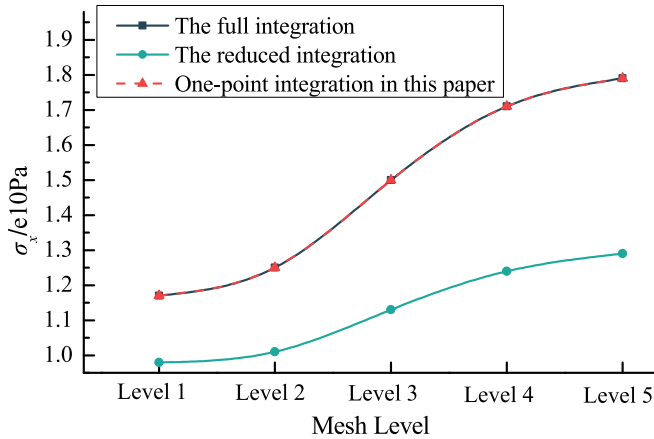
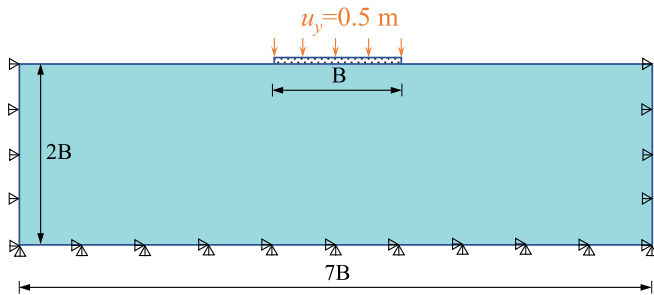
In computational mechanics, stress concentration is a critical



**Table 3**The comparison of stress component  $\sigma_x$  in point A.

Mesh level	The full integration	The reduced integration		One-point integration in this paper	
		$\sigma_x$ /10ePa	Error <sup>a</sup> /%	$\sigma_x$ /10ePa	Error <sup>b</sup> /%
1	1.17	0.98	16.24	1.17	0
2	1.25	1.01	19.20	1.25	0
3	1.50	1.13	25.67	1.50	0
4	1.71	1.24	27.49	1.71	0

<sup>a,b</sup> Errors of the reduced and one-point integration with the full integration for the same mesh.

**Fig. 12.**  $\sigma_x$  of point A versus mesh level of different integration schemes.**Fig. 13.** Strip foundation and soil model.

phenomenon that exhibits particular sensitivity to numerical integration schemes. To illustrate the performance of the one-point integration scheme presented herein, this study employs a benchmark problem that involves stress concentration.

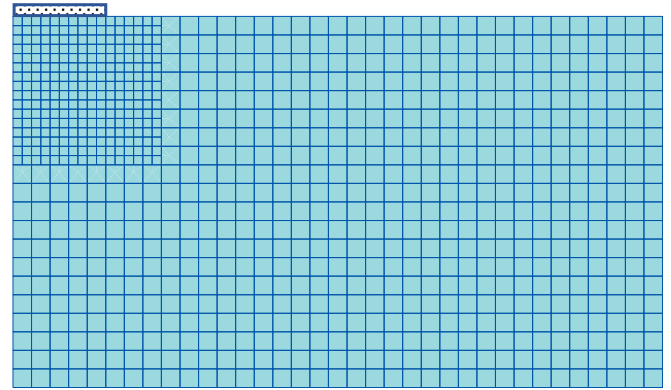
#### 4.2.1. Model information

In this section, a square plate with a circular hole at its center, which is shown in Fig. 9, is employed as a benchmark example to investigate the stress concentration behavior under biaxial loading. The geometry consists of a 2D square domain with edge length  $L = 10$  m, containing a concentric circular hole of radius  $R = 1$  m, where the ratio  $R/L$  is maintained at 0.2 to ensure proper stress concentration effects. The plate is subjected to uniform tensile stress  $q = 6e8$  Pa along the  $x$ -direction at both ends, while remaining stress-free along the  $y$ -direction boundaries, creating a biaxial stress state in the vicinity of the hole. The material is considered to be isotropic and linearly elastic, with a Young's modulus of  $E = 210$  GPa and a Poisson's ratio of  $\nu = 0.3$ . These material parameters are selected to represent typical engineering materials,

**Table 4**

Material parameters of the perfect elastic–plastic soil.

$c$ /kPa	$\phi$ (°)	$\psi$ (°)	$\gamma$ (kN/m <sup>3</sup> )	$E$ /MPa	$\nu$
1.0	0	0	2.360	0.5	0.49

**Fig. 14.** The discretized quadtree mesh for strip foundation and soil model.

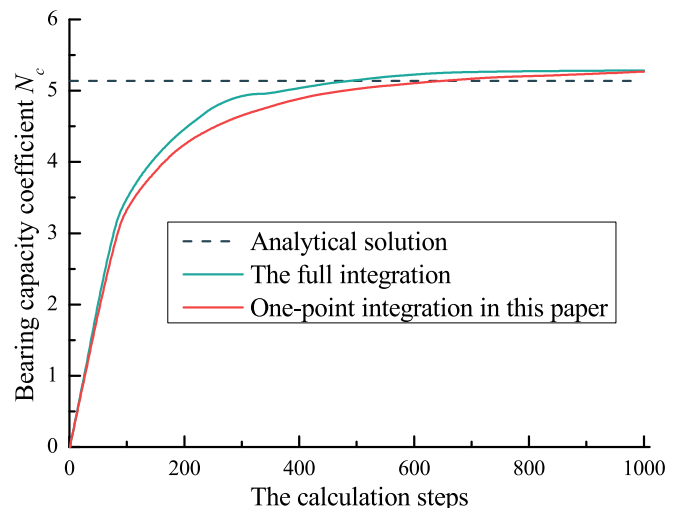
ensuring the results are applicable to practical scenarios.

#### 4.2.2. Mesh discretization

To systematically evaluate the performance of the one-point integration scheme in this paper under varying levels of mesh, five distinct mesh configurations with different levels (see Fig. 10), which include 282, 1152, 2592 and 4608 elements, are generated. These meshes are specifically designed to accurately capture the stress distribution around the edge of hole, where the stress concentration is most pronounced. Meanwhile, this progressive mesh refinement is implemented to achieve a converged solution and to obtain the theoretical stress distribution along the hole boundary. The finest mesh level, consisting of 4608 elements, is employed as the reference solution to validate the results from coarser meshes.

#### 4.2.3. Calculated stress results and comparison

Numerical simulations using three integration schemes, i.e., the full integration scheme, the reduced integration scheme, and the proposed linearly consistent one-point integration scheme in this paper, based on different mesh levels are performed, and the contours of the stress component  $\sigma_x$  obtained from the calculation of the finest mesh with level

**Fig. 15.** Comparison of  $N_c$  for different integration schemes.

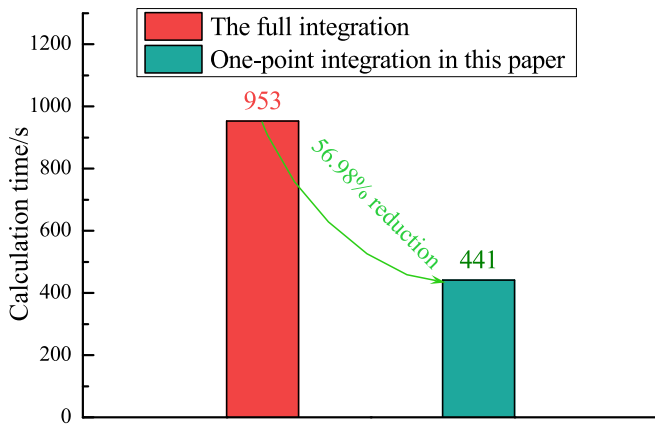


Fig. 16. Comparison of calculation times for different integration schemes.

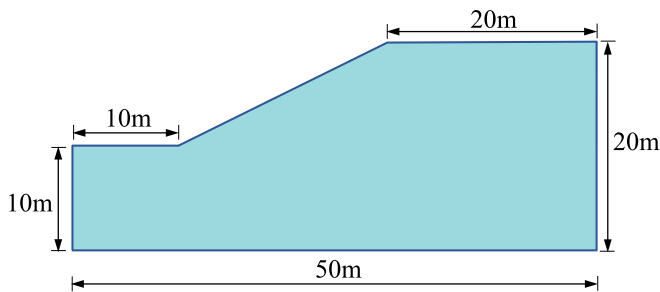


Fig. 17. The slope model.

4 are shown in Fig. 11. As can be seen from Fig. 11, stress concentration occurs at the top and bottom of the circular hole due to the geometry and loading conditions.

Further, we selected point A, which is marked in Fig. 9, at the upper edge of the hole, which has the largest change in strain gradient, as the observation point. The stress values at point A obtained for the simulation of the three integration schemes are listed in Table 3 and Fig. 12. The full integration results serve as the reference solution for comparison.

The analysis reveals obvious deviations between the stress solutions obtained using reduced integration scheme and those from the full integration scheme. Regardless of the mesh density, the errors in the stress solutions computed by the reduced integration scheme exceed 15 % compared to the full integration results. Moreover, as the mesh density increases, these errors exhibit an increasing trend rather than converging toward the reference solution. This phenomenon originates from the numerical instability inherent in the reduced integration scheme, which fails to adequately capture the stress gradients near the hole's edge because of insufficient sampling points. Consequently, the reduced integration scheme produces substantial inaccuracies in regions with high stress gradients.

In contrast, the one-point integration scheme in this paper demonstrates remarkable accuracy and consistency. Despite fewer integration points are employed, it achieves stress solutions identical to those of the full integration scheme at all mesh levels. The presented example demonstrates that the one-point integration scheme eliminates the intrinsic constraints of conventional reduced integration schemes while retaining the computational simplicity of one single integration point scheme. Thus, this approach offers a robust and reliable computational framework for accurately predicting stress concentration phenomenon, making it particularly well-suited for practical engineering applications.

Table 5

Material parameters of the slope filling soil.

$c/\text{kPa}$	$\varphi/(^{\circ})$	$\psi/(^{\circ})$	$\gamma/(\text{KN}/\text{m}^3)$	$E/\text{MPa}$	$\nu$
10	20	0	20	200	0.4

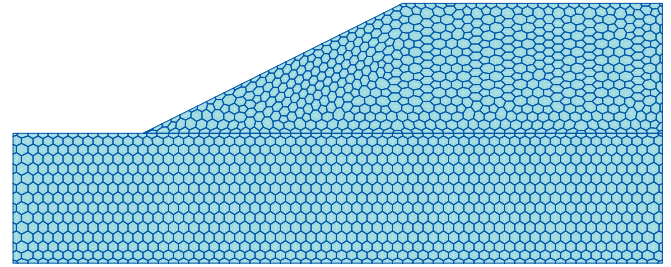


Fig. 18. The polygon mesh for the slope model.

### 4.3. Strip foundation bearing capacity

#### 4.3.1. Model information

The present example investigates the ultimate bearing capacity of a strip foundation resting on a perfect elastic–plastic soil, which is a classical example first studied by Prandtl (1920). A 2D numerical model (Fig. 13) is established, where the strip footing has a width of  $B = 10$  m. The soil domain extended to a depth of  $2B$  and a width of  $7B$ , ensuring minimal boundary effects on the results. The soil is modeled as a perfect elastic–plastic material following an associated flow rule, with a Mohr–Coulomb failure criterion governing its plastic behavior, and the material parameters are given in Table 4. The strip foundation is subjected to a uniform vertical displacement of  $u_y = 0.5$  m, and boundary conditions are also applied as depicted in Fig. 13.

#### 4.3.2. Calculation results

Given the symmetry, only half of the model is discretized, a quadtree computational mesh with 892 elements and 964 nodes is generated, which has been shown in Fig. 14. The size of quadrilateral elements far away from the strip foundation is  $1 \text{ m} \times 1 \text{ m}$ , while the soil near the strip foundation is refined into the mesh of  $0.5 \text{ m} \times 0.5 \text{ m}$ . According to the derivation of Prandtl (1920), the analytical value of ultimate bearing capacity  $N_c$  can be expressed as:

$$N_c = \left[ e^{\pi \tan \varphi} \tan^2 \left( \frac{\pi}{4} + \frac{\varphi}{2} \right) - 1 \right] \cot \varphi \quad (49)$$

For this example, the ultimate bearing capacity of the soil can be analytically calculated as  $N_c = 5.14$ . The SBFEM calculation applying full integration scheme and the one-point integration scheme in this paper is performed, where the vertical displacement is gradually applied in 1000 steps.

The bearing capacity coefficient  $N_c$ , calculated for both the full and the proposed one-point integration schemes, are plotted against the number of computation steps in Fig. 15. The figure shows that the curves between the two methods fit well, and as the number of computation steps increases, the bearing capacity coefficients  $N_c$  eventually converge to values closer to the analytical solution, with 5.28 for the full integration scheme and 5.27 for the one-point integration scheme in this paper. The computational time required for the two methods is 960 s and 413 s, respectively, as illustrated in Fig. 16. The results show that the one-point integration scheme in this paper is able to obtain a computational accuracy comparable to that of the full integration scheme, however, the computation time can be reduced by 56.98 %.

## 5. An application of slope stability

This section presents a static slope stability analysis to illustrate the

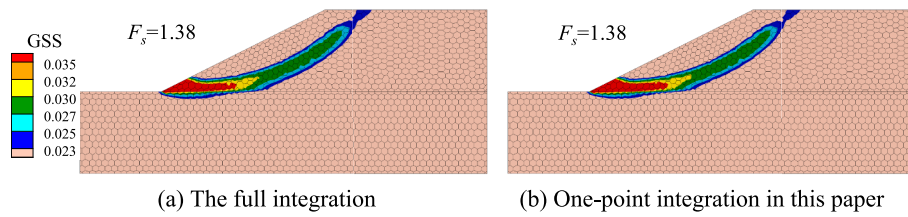


Fig. 19. The slip failure for different integration schemes.

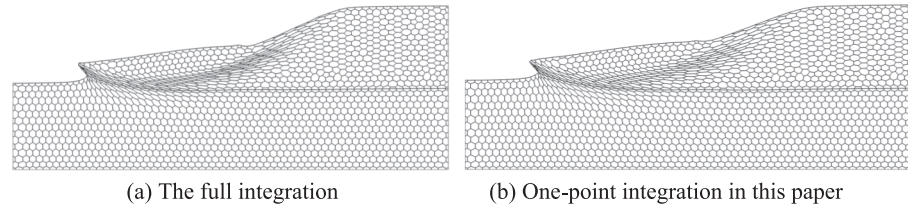


Fig. 20. Mesh deformation (magnification: 50) for two integration schemes.

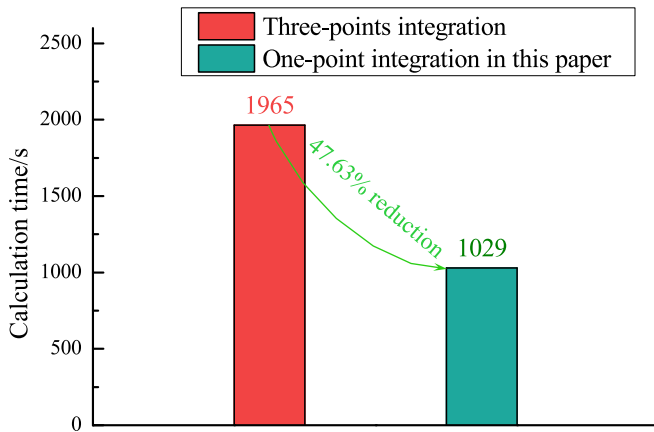


Fig. 21. Comparison of calculation times for different integration schemes.

application of the proposed method to actual geotechnical structures. The slope has a height of 10 m and a horizontal length of 10 m with a slope angle of  $45^\circ$ , as shown in Fig. 17. Other model information can also be obtained from the figure. At the left and right vertical boundary, a fixed horizontal displacement constraint ( $u_x = 0$ ) is imposed to prevent rigid body motion in the x-direction, while the bottom boundary is fully constrained ( $u_x = u_y = 0$ ). The slope is only subject to the force of its own gravity. The soil material of the slope follows a perfectly elastic–plastic Mohr–Coulomb constitutive model with a non-associated flow rule. The key material properties are summarized in Table 5. The slope model is discretized into a mesh comprising 1,636 polygonal elements and 3,224 nodes, as illustrated in Fig. 18.

The initial stress induced by self-weight is first established through SBFEM simulation. Following this, SBFEM analysis is performed with 5000 calculation steps, and multiple strength reduction calculations yield the safety factor of  $F_s = 1.38$  for the slope. Figs. 19–20 shows the slip surface and mesh deformation of the slope at the limit state obtained by two integration schemes, where the slip surface is characterized by the generalized shear strain (GSS). The analysis reveals a high degree of consistency between the two methods in assessing the two major slope stability indicators: the safety factor and the location of the slip surface. This consistency demonstrates the good validity and applicability of the one-point integration scheme in this paper in slope stability analysis. Comparison of calculation times for the two integration schemes are illustrated in Fig. 21. Compared to the full integration scheme, the one-

point integration scheme offers superior computational efficiency, with a reduction of 47.63 % in computation time, which is a satisfactory computational improvement.

Finally, the one-point integration scheme in this paper demonstrates a notable efficiency advantage in the elastic–plastic calculation of large-scale structures, and it has good application prospects in large-scale geotechnical engineering problems.

## 6. Conclusion

In this paper, the linearly consistent one-point integration scheme is extended to 2D SBFEM to integrate arbitrary polygons. The compatible strain in each sub-triangle domain is smoothed by the linear strain smoothing technique, following which the derivatives of the smoothed nodal shape functions are computed via a discrete form of the divergence theorem at the geometric center of sub-triangle domain. Stabilization is implemented by incorporating higher-order derivative terms into the formulation to ensure computational reliability. The accuracy and the applicability of the proposed method are evaluated through several examples in elastic and elastoplastic problems. The principal conclusions are outlined below:

- 1) The proposed one-point integration scheme within the SBFEM framework achieves acceptable computational accuracy. Despite employing only one integration point, the method maintains computational precision comparable to that of full integration scheme. Numerical examples reveal that the maximum error of the proposed method is merely 0.16 %, this exceptional accuracy is facilitated by the rigorous mathematical derivation underpinning the method, which effectively eliminates numerical instability issues commonly associated with reduced integration scheme.
- 2) Compared to the existing method, the proposed method demonstrates an enhanced computational efficiency. The reduction in the number of integration points effectively minimizes the time required for constitutive integration calculations, resulting in 45–60 % savings in computational time, thereby offering a robust and efficient solution in numerical simulation.
- 3) The application prospects of this method for large-scale engineering applications have been revealed. SBFEM enables flexible polygon elements to be solved directly, ensuring good mesh applicability to complex structures; Besides, the efficiency advantage of the proposed method is expected to be further pronounced in large-scale engineering calculations, offering substantial application value.

The one-point integration scheme for each subdomain of SBFEM proposed in this paper can be further extended to 3D SBFEM, and its efficiency enhancement will be more significant, which is also a focus of our future research.

### CRedit authorship contribution statement

**Xiupeng Nie:** Writing – review & editing, Writing – original draft, Validation, Software, Methodology, Investigation, Formal analysis. **Degao Zou:** Supervision, Resources, Funding acquisition, Conceptualization. **Kai Chen:** Writing – review & editing, Methodology. **Jingmao Liu:** Software, Resources. **Shanlin Tian:** Software, Investigation.

### Declaration of competing interest

The authors declare that they have no known competing financial interests or personal relationships that could have appeared to influence the work reported in this paper.

### Acknowledgements

This work was supported by the National Natural Science Foundation of China (Grant Nos. 52192674, 52350393) and the National Key R&D Program of China (2024YFF1702001).

### Data availability

Data will be made available on request.

### References

- Chen, K., Zou, D.G., Kong, X.J., Chan, A., Hu, Z.Q., 2017. A novel nonlinear solution for the polygon scaled boundary finite element method and its application to geotechnical structures. *Comput. Geotech.* 82, 201–210. <https://doi.org/10.1016/j.compgeo.2016.09.013>.
- Chen, K., Zou, D.G., Kong, X.J., Yu, X., 2018a. An efficient nonlinear quadtree SBFEM and its application to complicated geotechnical structures. *Comput. Geotech.* 96, 226–245. <https://doi.org/10.1016/j.compgeo.2017.10.021>.
- Chen, K., Zou, D.G., Kong, X.J., Zhou, Y., 2018b. Global concurrent cross-scale nonlinear analysis approach of complex CFRD systems considering dynamic impervious panel-rockfill material-foundation interactions. *Soil Dyn. Earthq. Eng.* 114, 51–68. <https://doi.org/10.1016/j.soildyn.2018.06.027>.
- Chen, K., Zou, D.G., Tang, H.X., Liu, J.M., Zhuo, Y., 2021. Scaled boundary polygon formula for Cosserat continuum and its verification. *Eng. Anal. Bound. Elem.* 126, 136–150. <https://doi.org/10.1016/j.enganabound.2021.02.007>.
- Chen, K., Zou, D.G., Yi, G.Y., Nie, X.P., Qu, Y.Q., 2024. A flexible mixed-order formula for tetrahedron elements based on SBFEM. *Comput. Geotech.* 171, 106390. <https://doi.org/10.1016/j.compgeo.2024.106390>.
- Cook, R.D., Saunders, H., Asme, 1984. Concepts and applications of Finite Element Analysis. *J. Pressure Vessel Technol.* 106 (1), 127. <https://doi.org/10.1115/1.3264300>.
- Du, C.B., Zhao, W.H., Jiang, S.Y., Deng, X.D., 2020. Dynamic XFEM-based detection of multiple flaws using an improved artificial bee colony algorithm. *Comput. Method. Appl. M.* 365, 112995. <https://doi.org/10.1016/j.cma.2020.112995>.
- Du, C.B., Huang, W.C., Ghaemian, M., Jiang, S.Y., Zhao, Z.W., 2023. New nonlocal multiscale damage model for modelling damage and cracking in quasi-brittle materials. *Eng. Fract. Mech.* 277, 108927. <https://doi.org/10.1016/j.engfracmech.2022.108927>.
- Duan, Q.L., Belytschko, T., 2009. Gradient and dilatational stabilizations for stress-point integration in the element-free Galerkin method. *Int. J. Numer. Meth. Eng.* 77, 776–798. <https://doi.org/10.1002/nme.2432>.
- Duan, Q.L., Li, X.K., Zhang, H.W., Wang, B.B., Gao, X., 2012a. Quadratically consistent one-point (QC1) quadrature for meshfree Galerkin methods. *Comput. Method. Appl. M.* 245, 256–272. <https://doi.org/10.1016/j.cma.2012.07.019>.
- Duan, Q.L., Li, X.K., Zhang, H.W., Belytschko, T., 2012b. Second order accurate derivatives and integration schemes for meshfree methods. *Int. J. Numer. Meth. Eng.* 92, 399–424. <https://doi.org/10.1002/nme.4359>.
- Duan, Q.L., Gao, X., Wang, B.B., Li, X.K., Zhang, H.W., Belytschko, T., Shao, Y.L., 2014. Consistent elementfree Galerkin method. *Int. J. Numer. Meth. Eng.* 99 (2), 79–101. <https://doi.org/10.1002/nme.4661>.
- Flanagan, D.P., Belytschko, T., 1981. A uniform strain hexahedron and quadrilateral with orthogonal hourglass control. *Int. J. Numer. Meth. Eng.* 17 (5), 679–706. <https://doi.org/10.1002/nme.1620170504>.
- Fries, T.P., Belytschko, T., 2008. Convergence and stabilization of stress-point integration in mesh-free and particle methods. *Int. J. Numer. Meth. Eng.* 74, 1067–1087. <https://doi.org/10.1002/nme.2198>.
- Gao, X., Duan, Q.L., Shao, Y.L., Li, X.K., Chen, B.S., Zhang, H.W., 2016. Quadratically consistent one-point (QC1) integration for three-dimensional element-free Galerkin method. *Finite Elem. Anal. Des.* 114, 22–38. <https://doi.org/10.1016/j.finel.2016.01.003>.
- Hughes, T.J.R., Cohen, M., Haroun, M., 1978. Reduced and selective integration techniques in the finite element analysis of plates. *Nucl. Eng. Des.* 46 (1), 203–222. [https://doi.org/10.1016/0029-5493\(78\)90184-X](https://doi.org/10.1016/0029-5493(78)90184-X).
- Kie, C.K., Sang, H.P., Sung, K.Y., 2006. The support integration scheme in the least-squares mesh-free method. *Finite Elem. Anal. Des.* 43, 127–144. <https://doi.org/10.1016/j.finel.2006.08.005>.
- Liu, G.R., Dai, K.Y., Nguyen, T.T., 2007. A smoothed finite element method for mechanics problems. *Comput. Mech.* 39, 859–877. <https://doi.org/10.1007/s00466-006-0075-4>.
- Liu, Y., Belytschko, T., 2010. A new support integration scheme for the weak form in mesh-free methods. *Int. J. Numer. Meth. Eng.* 82, 699–715. <https://doi.org/10.1002/nme.2780>.
- Liu, J., Hao, C.K., Ye, W.B., Yang, F., Lin, G., 2021. Free vibration and transient dynamic response of functionally graded sandwich plates with power-law nonhomogeneity by the scaled boundary finite element method. *Comput. Method. Appl. M.* 376, 113665. <https://doi.org/10.1016/j.cma.2021.113665>.
- Long, Y.Q., Xu, Y., 1994. Generalized conforming triangle membrane element with vertex rigid rotational freedoms. *Finite Elem. Anal. Des.* 17 (4), 259–271. [https://doi.org/10.1016/0168-874X\(94\)90002-7](https://doi.org/10.1016/0168-874X(94)90002-7).
- Nie, X.P., Zou, D.G., Chen, K., Kong, X.J., Yi, G.Y., 2024a. A SBFEM formula for the mixed-order hexahedron interpolation based on serendipity elements. *Eng. Anal. Bound. Elem.* 164, 105760. <https://doi.org/10.1016/j.enganabound.2024.105760>.
- Nie, X.P., Zou, D.G., Chen, K., Yi, G.Y., Kong, X.J., 2024b. An improved high-precision polyhedron SBFEM with combinatorial interpolation strategies. *Eng. Anal. Bound. Elem.* 169, 105991. <https://doi.org/10.1016/j.enganabound.2024.105991>.
- Nie, X.P., Zou, D.G., Chen, K., Liu, J.M., Kong, X.J., Qu, Y.Q., 2024c. The versatile polyhedral elements of Cosserat continuum theory based on SBFEM and its application. *Eng. Anal. Bound. Elem.* 162, 87–101. <https://doi.org/10.1016/j.enganabound.2024.02.001>.
- Ooi, E.T., Man, H., Natarajan, S., Song, C.M., 2015. Adaptation of quadtree meshes in the scaled boundary finite element method for crack propagation modelling. *Eng. Fract. Mech.* 144, 101–117. <https://doi.org/10.1016/j.engfracmech.2015.06.083>.
- Ooi, E.T., Song, C.M., Natarajan, S., 2016. Construction of high-order complete scaled boundary shape functions over arbitrary polygons with bubble functions. *Int. J. Numer. Meth. Eng.* 108 (9), 1086–1120. <https://doi.org/10.1002/nme.5259>.
- Ooi, E.T., Song, C.M., Natarajan, S., 2018. A scaled boundary finite element formulation for poroelasticity. *Int. J. Numer. Meth. Eng.* 114 (8), 905–929. <https://doi.org/10.1002/nme.5770>.
- Ooi, E.T., Saputra, A., Natarajan, S., Ooi, E.H., Song, C.M., 2020. A dual scaled boundary finite element formulation over arbitrary faceted star convex polyhedra. *Comput. Mech.* 66, 27–47. <https://doi.org/10.1007/s00466-020-01839-9>.
- Prandtl, L., 1920. Über die härte plastischer körper, *Nachrichten von der Gesellschaft der Wissenschaften zu Göttingen. Mathematisch-Physikalische Klasse* 12, 74–85.
- Song, C.M., Wolf, J.P., 1997. The scaled boundary finite-element method—alias consistent infinitesimal finite-element cell method—for elastodynamics. *Comput. Method. Appl. M.* 147 (3–4), 329–355. [https://doi.org/10.1016/S0045-7825\(97\)00021-2](https://doi.org/10.1016/S0045-7825(97)00021-2).
- Song, C.M., Wolf, J.P., 1998. The scaled boundary finite-element method: analytical solution in frequency domain. *Comput. Method. Appl. M.* 164 (1), 249–264. [https://doi.org/10.1016/S0045-7825\(98\)00058-9](https://doi.org/10.1016/S0045-7825(98)00058-9).
- Song, C.M., 2004. A matrix function solution for the scaled boundary finite-element equation in statics. *Comput. Method. Appl. M.* 193 (23–26), 2325–2356. <https://doi.org/10.1016/j.cma.2004.01.017>.
- Song, C.M., 2009. The scaled boundary finite element method in structural dynamics. *Int. J. Numer. Meth. Eng.* 77 (8), 1139–1171. <https://doi.org/10.1002/nme.2454>.
- Song, C.M., Tin-Loi, F., Gao, W., 2010. Transient dynamic analysis of interface cracks in anisotropic bimaterials by the scaled boundary finite-element method. *Int. J. Solids Struct.* 47 (7–8), 978–989. <https://doi.org/10.1016/j.ijsolstr.2009.12.015>.
- Song, C.M., Ooi, E.T., Natarajan, S., 2018. A review of the scaled boundary finite element method for two-dimensional linear elastic fracture mechanics. *Eng. Fract. Mech.* 187, 45–73. <https://doi.org/10.1016/j.engfracmech.2017.10.016>.
- Wang, B.B., Lu, C.S., Fan, C.Y., Zhao, M.H., 2019. Consistent integration schemes for meshfree analysis of strain gradient elasticity. *Comput. Method. Appl. M.* 357, 112601. <https://doi.org/10.1016/j.cma.2019.112601>.
- Ye, W.B., Zang, Q.S., Liu, J., Yang, F., Lin, G., 2023. Three-dimensional bending and free vibration analyses of laminated cylindrical panel with/without elastic foundation using two-dimensional discrete method. *Soil Dyn. Earthq. Eng.* 168, 107831. <https://doi.org/10.1016/j.soildyn.2023.107831>.
- Zhang, P., Du, C.B., Birk, C., Zhao, W.H., 2019. A scaled boundary finite element method for modelling wing crack propagation problems. *Eng. Fract. Mech.* 216, 106466. <https://doi.org/10.1016/j.engfracmech.2019.04.040>.
- Zhang, G.L., Zhao, M., Huang, J.Q., Du, X.L., Zhao, X.L., 2021a. A substructure method for underground structure-dry soil-saturated soil-bedrock interaction under obliquely incident earthquake and its application to groundwater effect on tunnel. *Tunn. Undergr. Sp. Tech.* 111, 103864. <https://doi.org/10.1016/j.tust.2021.103864>.
- Zhang, P., Du, C.B., Zhao, W.H., Sun, L.G., 2021b. Dynamic crack face contact and propagation simulation based on the scaled boundary finite element method. *Comput. Method. Appl. M.* 385, 114044. <https://doi.org/10.1016/j.cma.2021.114044>.



- Zhang, G.L., Zhao, M., Du, X.L., Zhang, J.Q., 2023a. Time-domain scaled boundary perfectly matched layer for elastic wave propagation. *Int. J. Numer. Meth. Eng.* 124, 3906–3934. <https://doi.org/10.1002/nme.7300>.
- Zhang, G.L., Zhao, M., Zhang, J.Q., Du, X.L., 2023b. Scaled boundary perfectly matched layer (SBPML): a novel 3D time-domain artificial boundary method for wave problem in general-shaped and heterogeneous infinite domain. *Comput. Method. Appl. M.* 403, 115738. <https://doi.org/10.1016/j.cma.2022.115738>.
- Zhang, G.L., Zhao, M., Zhang, J.Q., Wang, J.T., Du, X.L., 2024a. Scaled boundary perfectly matched layer for wave propagation in a three-dimensional poroelastic medium. *Appl. Math. Model.* 125, 108–138. <https://doi.org/10.1016/j.apm.2023.09.028>.
- Zhang, G.L., Zhao, M., Zhang, J.Q., Du, X.L., 2024b. Prismatic-element SBPML coupled with SBFEM for 3D infinite transient wave problems. *Comput. Method. Appl. M.* 427, 117014. <https://doi.org/10.1016/j.cma.2024.117014>.
- Zhang, J.R., Zhao, M., Zhang, G.L., Zhang, J.Q., Du, X.L., 2024c. 3D acoustic scaled boundary perfectly matched layer (SBPML) for acoustic-structure interaction problems. *Eng. Anal. Bound. Elem.* 164, 105765. <https://doi.org/10.1016/j.enganbound.2024.105765>.
- Zhao, W.H., Du, C.B., Jiang, S.Y., 2018. An adaptive multiscale approach for identifying multiple flaws based on XFEM and a discrete artificial fish swarm algorithm. *Comput. Method. Appl. M.* 339, 341–357. <https://doi.org/10.1016/j.cma.2018.04.037>.
- Zhao, M., Zhang, G.L., Wang, P.G., Du, X.L., Zhang, X.L., 2020. An accurate frequency-domain model for seismic responses of breakwater-seawater-seabed-bedrock system. *Ocean Eng.* 197, 106843. <https://doi.org/10.1016/j.oceaneng.2019.106843>.
- Zhuo, Y., Zou, D.G., Chen, K., Qu, Y.Q., Yi, G.Y., Tian, S.L., 2025. Improved double-phase-field algorithm based on scaled boundary finite element method for rock-like materials. *Theor. Appl. Fract. Mec.* 138, 104916. <https://doi.org/10.1016/j.tafmec.2025.104916>.
- Zienkiewicz, O.C., Taylor, R.L., Too, J.M., 1971. Reduced integration technique in general analysis of plates and shells. *Int. J. Numer. Meth. Eng.* 3 (2), 275–290. <https://doi.org/10.1002/nme.1620030211>.
- Zou, D.G., Kong, X.J., Liu, J., et al., 2022. Theoretical introduction and user manual of the GEODYNA7.0: a high-performance finite element analysis software system for large-scale geotechnical engineering. Dalian University of Technology, Dalian.